Thesis for the degree
Master of Science

Submitted to the Scientific Council of the
Weizmann Institute of Science
Rehovot, Israel

עבודת גמר (תזה) לתואר
מוסמך למדעים

מוגשת למועצה המדעית של
מכון ויצמן למדע
רחובות, ישראל

By
Dror Einav

מאת
דרור עינב

אפיון מלכודת פול לינארית כבסיס לשליטה קוונטית במולקולות

The Characterization of a Linear Paul Trap, Towards Molecular Quantum Control

Advisor:
Ziv Meir

מנחה:
זיו מאיר

Month and Year
March 2025

חודש ושנה עבריים
אדר תשפ"ה

Abstract

Trapped ions are a leading platform for quantum technologies and the fundamental study of quantum mechanics. By using Paul traps, state-of-the-art fidelity of coherent quantum control operations can be achieved with trapped ions. Additionally, methods unique to trapped ions, such as quantum logic, allow for precise control over a wide range of atomic species. Recently, this approach was used for the first time to achieve coherent quantum control over molecular ions.

In this work, we characterized a linear Paul trap, paving the way for molecular quantum control. Our initial goal was to make the trap's confinement tight enough to prevent ion motion from causing dephasing—specifically, to bring the trap into the Lamb-Dicke regime. A comparison between the measured trapping frequencies and theoretical calculations revealed that structural asymmetries in our trap distort the ideal symmetric potential. Furthermore, an avoided-crossing behavior was observed between the two radial trapping frequencies, suggesting that two of the trapping quadrupoles are coupled. This phenomenon is not yet fully understood and will be further studied by our group.

In addition, we've studied the stability of the radial frequencies and their dependence on the helical resonator, which induces the radio frequency (RF) voltage on the trap's electrodes. The maximal transmitted RF power and the minimal reflected RF power were measured for different RF frequencies, with the former ensuring that the radial frequencies are least sensitive to resonator-induced noise. To further stabilize the radial trapping frequencies, a digital PID control system was implemented.

Finally, we present some of the challenges encountered in the early days of our group. We designed and built an optical table to support the Paul trap's vacuum chamber and the surrounding optical setup. The table was designed to meet the constraints imposed by the vacuum chamber and the molecular beam machine while ensuring compatibility with future experiments. Building and successfully re-trapping ions within it mark the beginning of our transition from a new research group to an established experimental lab.

Acknowledgments

Throughout this thesis, the pronoun "I" is used in this section alone, as the work presented here was made possible by the efforts of many others. The solid foundations laid by Orr Barnea, Idan Hochner, and Jonas Drotleff - who were the first to trap ions in our group a short time before I joined - were essential to this project, which ultimately completed what they started. The supportive atmosphere in our group, shaped by them and my other lab mates - Mai Faibish, Tom Shahaf, Rukmini Harale, and Evgenii Kipiatkov, allowed me to freely ask questions and seek advice on anything. I want to thank all of you for being the ideal company to do science with, and for never leaving me alone at lunch.

Beyond my lab mates, our group wouldn't be the same without the patient guidance and support of our supervisor, Ziv Meir. It is rare to find a supervisor who is involved even in the smallest of details and always makes time to provide hands-on guidance with infectious enthusiasm.

Special thanks to the employees of the Department of Physics of Complex Systems workshop. In their professional work, they have guided me to ask the right questions and were always happy to assist.

I want to thank my family and my partner, Eden, for putting up with me in my years of study, especially in the past months of writing.

The work described in this thesis was mainly done in the seventeen months following October 7, 2023. I want to acknowledge all those who have fought to secure the release of the innocents kidnapped on that cursed day. Your efforts have allowed us to live normal lives and pursue scientific research. I sincerely hope that by the time these words are read, all the hostages have safely returned home.

List of Abbreviations

RF - Radio frequency
DC - Direct current
MMC - Micromotion compensation
EMM - Excess micromotion
PS - Power supply
AM - Amplitude modulation
std - standard deviation
PID - proportional–integral–derivative

Contents

Introduction

Over a century since it was first formulated, quantum mechanics remains one of the most intriguing theories in modern science. The study of quantum mechanics enabled a better understanding of nature's fundamental building blocks and stands on the basis of science's most accurate predictions. The unique and unintuitive phenomena it reveals, such as superposition and entanglement, are utilized to achieve advanced technologies such as atomic clocks [1] and quantum computers [2]. Despite the countless achievements the scientific community had in the study of quantum mechanics, many questions remained open.

Cold atoms and atomic ions were proven to be one of the most fruitful platforms in the study of quantum mechanics [3] and quantum technologies. One such application of cold atoms in modern technology is ultra-stable atomic clocks, which are state-of-the-art in time-keeping [4]. The great advancements in this field required the development of new quantum control methods, enabling the study of a broader range of atomic species with improved accuracy.

Only in the past two decades, the techniques developed in the field of cold atoms were successfully used to demonstrate quantum control of molecules and molecular ions [5–7]. Molecules are advantageous to atoms in their diversity and range of sizes, compositions, and weights. They also hold unique characteristics due to their complex structure and additional degrees of freedom. The field of quantum control of molecules holds many prospects, such as new types of quantum superpositions [8], studies of many-body physics, molecular metrology [9, 10], and many others. These make molecules attractive candidates for emerging quantum technologies.

The appealing features of molecules also impose challenges in molecular quantum control. Due to their complex energy structure, most molecules lack closed transitions for laser cooling and detection [11]. Since particles must be sufficiently cold and isolated for their quantum mechanical nature to be observed, other techniques must be used in molecular quantum control. Furthermore, most state detection methods used for molecules involve state-destructive processes, like photodissociation or chemical reactions, thus restricting molecules as a platform for quantum technologies. Both issues can be solved by co-trapping molecular and atomic ions and utilizing their Coulomb interaction for cooling and state detection. This technique, called "quantum logic", is widely used with atomic pairs and was demonstrated to be effective in the cooling of the external degrees of freedom in molecules [5] and for non-demolition state detection [7].

A pre-requisite to molecular quantum control via quantum-logic is the ability to trap and manipulate a single atom. Using RF Paul traps [12], atomic ions can be stored for days, and can be manipulated with exceptionally high operation fidelity [13]. For a Paul trap to facilitate quantum control and quantum logic, it must be sufficiently tight [14]. This condition, called the Lamb-Dicke regime, ensures that the motion of the ion in the trap will not cause decoherence. Moreover, the ion's modes of motion inside a trap tuned to the Lamb-Dicke regime are crucial in the application of quantum-logic.

This thesis presents the mapping of the parameter space of an RF Paul trap, by measuring the trapping frequencies of a single Ca^+ ion. These measurements allow us to properly tune the Paul trap in our experimental setup into the Lamb-Dicke regime, setting the stage for quantum control, first in $^{40}Ca^+$ atomic ion, and later in N_2^+ molecular ion. The measurements are compared with the theoretical values, revealing interesting deviations from it, some due to structural asymmetries and some due to coupling between the

trapping electrical fields. The latter has yet to be fully understood.

Two additional projects are presented. The first presents the investigation of the stability of the radial trapping frequencies in our Paul trap, along with efforts to stabilize them using digital proportional–integral–derivative (PID) control. The PID control relied on the corelation between the induced RF power and the value of the radial trapping frequency. Although it is not fully operational, the insights gained along the PID implementation processes were useful to our daily experimental routine. The second project presents the design and construction of the optical setup around our ion trap, considering the constraints imposed by the vacuum system, in which the trap is placed.

Goals

In MoleQuLab, we wish to create a MoleQubits - an isolated two-level system in a molecule with preparation, detection, and coherent control capabilities - to study molecules' quantum mechanical nature and to utilize them for future technologies. We will use quantum-logic as the primary technique for cooling and state detection. In this technique, a "logical" ion is co-trapped with the "qubit" ion in a radio-frequency (rf) trap, such that the qubit is being manipulated by the logical ion[15]. To facilitate the quantum-logic, we've built a linear Paul trap and trapped a single Ca^+ ion that is cooled via Doppler cooling.

The goal of this work was to bring a functional ion trap into the Lamb-Dicke regime, allowing it to facilitate quantum control operations. We aimed to characterize the trapping frequencies as a function of various trapping parameters to identify optimal conditions for different applications, such as ion loading and quantum control. For that, tickle measurement was implemented and validated in our setup. The measurements were compared with theoretical calculations for further study of our Paul trap.

As a new lab, an additional goal was to transition our experimental setup from temporary rooms to our permanent lab. Our aim was to design and construct the apparatus in its complete form, accounting for future setups as well. This work lays the foundations for molecular quantum control.

Methods

Linear Paul Trap

Earnshaw's theorem teaches us that nature does not allow a fully electrostatic trapping potential. To overcome this challenge, Wolfgang Paul presented the idea of time-dependent electrical fields as the basis for ion traps [12], an idea that won him the 1989 Noble Prize. This type of traps, now known as Paul traps, use static electric potential - V_{DC} and a time-dependent electric potential - V_{RF} to allow trapping. In its linear form, the trap potential is

$$V_{\mathrm{lin}} = \frac{1}{2}V_{\mathrm{RF}}\left(1+\frac{x^2-y^2}{r_0^2}\right)\cos(\Omega_{\mathrm{rf}}t) - \frac{1}{2}V_{\mathrm{DC}}\frac{x^2+y^2-2z^2}{z_0^2}.$$

Here, Ω_{rf} is the RF frequency, and r_0 and z_0 are geometrical parameters of the trap. Using Newton's second law, one can write the equations of motion of a charged particle in the trap for each axis as

$$\frac{d^2x}{dt^2} = \frac{Z}{m}\left(V_{\mathrm{DC}}\frac{x}{z_0^2} - V_{\mathrm{RF}}\cos(\Omega_{\mathrm{rf}}t)\frac{x}{r_0^2}\right),$$

$$\frac{d^2y}{dt^2} = \frac{Z}{m}\left(V_{\mathrm{DC}}\frac{y}{z_0^2} + V_{\mathrm{RF}}\cos(\Omega_{\mathrm{rf}}t)\frac{y}{r_0^2}\right),$$

and

$$\frac{d^2z}{dt^2} = -\frac{Z}{m}V_{\mathrm{DC}}\frac{2z}{z_0^2}.$$

Here m is the particle's mass, and Z is the particle's electric charge. From now on, we will use $Z = e$ as the charge of our ion (e is the elementary charge) - as this is the case in our experiment.

By defining the dimensionless parameters

$$a = \frac{4eV_{\mathrm{DC}}}{m\Omega_{\mathrm{rf}}^2 z_0^2} \quad , \quad q = \frac{2eV_{\mathrm{RF}}}{m\Omega_{\mathrm{rf}}^2 r_0^2}, \tag{1}$$

we can rewrite the equations of motion in the form of the well-known Mathieu equation [16, 17]-

$$\frac{d^2u_i}{d\tau^2} + \left[a_i + 2q_i\cos(2\tau)\right]u_i = 0.$$

For $u_i = [x, y, z]$, $a_i = [-a, -a, 2a]$, $q_i = [q, -q, 0]$, and the dimensionless timescale $\tau = \Omega_{\mathrm{rf}}t$. In the limit $|a_i| \ll q_i^2 \ll 1$ the trajectories of the particles are

$$u_i(t) \approx u_0\cos(\omega_i t)\left[1+\frac{1}{2}q_i\cos(\Omega_{\mathrm{rf}}t)\right],$$

where,

$$\omega_i = \frac{1}{2}\Omega_{\mathrm{rf}}\sqrt{a_i + \frac{q_i^2}{2}}.$$

The trajectory of the ion is composed of two terms. The first, called the secular motion, involves harmonic oscillations with large amplitude corresponding to the pseudo-harmonic potential of the trap. Here,

the frequency of the secular motion in each axis is given by ω_i. For the trap to be stable, the condition $|2a| < q^2$ must be satisfied (otherwise, ω_i is imaginary). The second term, called micromotion, consists of fast oscillations with a small amplitude that are superimposed on top of the secular motion. It is essentially the driven motion of the ion caused by the oscillations of the RF field. We note that since the amplitude of the micromotion scale with q_i, the ion does not experience micromotion at the axial axis, as $q_z = 0$. In an ideal trap, the minimum of the pseudo-harmonic potential is located at the center of the trap, along the axial axis, where the RF-field nulls. In the lab, stray electric fields shift this stable point, causing excess micromotion (EMM). Applying an opposite field can negate this effect and reduce the EMM to a minimum.

The linear Paul trap has cylindrical symmetry:

$$(q_x^2 = q_y^2\ ,\ a_x = a_y) \rightarrow \omega_x = \omega_y.$$

As discussed later on, this symmetry may raise challenges for the laser cooling process. In order to break this symmetry, one can add a bias DC quadrupole, V_b, in the radial plane similar to the RF quadrupole, resulting in an asymmetric potential

$$V_{\text{lin}} = \frac{1}{2}V_{\text{RF}}\left(1 + \frac{x^2 - y^2}{r_0^2}\right)\cos(\Omega_{\text{rf}}t) - \frac{1}{2}V_{\text{DC}}\frac{x^2 + y^2 - 2z^2}{z_0^2} - \frac{1}{2}V_{\text{b}}\left(1 + \frac{x^2 - y^2}{r_0^2}\right). \tag{2}$$

The modified trap frequencies are

$$\omega_i = \frac{1}{2}\Omega_{\text{rf}}\sqrt{a_i + b_i + \frac{q_i^2}{2}}, \tag{3}$$

for $b_i = [-b, b, 0]$ where

$$b = \frac{4eV_b}{mr_0^2\Omega_{rf}^2}. \tag{4}$$

This configuration gives rise to three non-degenerate modes of motion: axial (ω_z), low radial (ω_-), and high radial (ω_+) modes. Measuring these frequencies can be done using "tickle" - exciting an ion in one of the mods via an oscillatory force at a frequency that resonates with the mode.

Lamb-Dicke Regime

In order to perform sideband cooling and state detection via quantum logic, we must be able to resolve the ion's sidebands and drive their transitions [15, 18]. To do so, we will work in the Lamb-Dicke regime, in which the ion is localized in the trap relative to the laser's wavelength $\Delta x \ll \lambda$. In this regime, the motion of the ion in the trap does not cause Doppler broadening, as the ion cannot accumulate a significant phase relative to the laser, and its motional sidebands are resolved. To see this, let us look at the Hamiltonian describing the system following [14, 19]. In the following discussion, we will focus on the axial axis since we plan to use only the axial modes in our upcoming experiments. Moreover, the trapping potential in the axial axis is purely harmonic such that the treatment is more exact.

The Hamiltonian of our system is

$$\hat{H} = \hat{H}^{(e)} + \hat{H}^{(m)} + \hat{H}^{(i)},$$

where

$$\hat{H}^{(e)} = \hbar\frac{\omega}{2}\hat{\sigma}_z,$$

and

$$\hat{H}^{(m)} = \hbar\omega_z(\hat{a}_z^\dagger\hat{a}_z + \frac{1}{2}).$$

The first term, $\hat{H}^{(e)}$, is the electronic Hamiltonian with $\hbar\omega$ the energy gap between the ion's ground and excited states, and σ_z the Pauli z matrix. The second term, $\hat{H}^{(m)}$, is the Paul trap Hamiltonian in the axial axis, which is a harmonic oscillator Hamiltonian since $q_z = 0$. The axial trapping frequency is ω_z, and $\hat{a}_z$ and $\hat{a}_z^\dagger$ are the annihilation and creation operators respectively. The last term, the interaction Hamiltonian, is given by

$$\hat{H}^{(i)} = \frac{\hbar\Omega}{2}(\hat{\sigma}_+ + \hat{\sigma}_-) \times (e^{i(k\hat{z}-\omega t)} + e^{-i(k\hat{z}-\omega t)}).$$

Here, Ω is the ions Rabi frequency, k is the laser wave vector (assuming it propagates along the z direction), and $\hat{\sigma}_\pm$ are its internal state's raising and lowering operators. Using the interaction free Hamiltonian, $\hat{H}_0 = \hat{H}^{(m)} + \hat{H}^{(e)}$, we can write the interaction Hamiltonian in the interaction picture,

$$\begin{aligned}
\hat{H}_{\text{int}} &= \hat{U}_0^\dagger\hat{H}^{(i)}\hat{U}_0 \\
&= \frac{\hbar\Omega}{2}(\hat{\sigma}_+e^{i\omega_0 t} + \hat{\sigma}_-e^{-i\omega_0 t})e^{\frac{i}{\hbar}\hat{H}^{(m)}t}(e^{i(k\hat{z}-\omega t)} + e^{-i(k\hat{z}-\omega t)})e^{-\frac{i}{\hbar}\hat{H}^{(m)}t} \\
&= \frac{\hbar\Omega}{2}(\hat{\sigma}_+e^{\frac{i}{\hbar}\hat{H}^{(m)}t}(e^{i(k\hat{z}-(\omega-\omega_0)t)} + e^{-i(k\hat{z}-(\omega+\omega_0)t)})e^{-\frac{i}{\hbar}\hat{H}^{(m)}t} \\
&\quad + \hat{\sigma}_-e^{\frac{i}{\hbar}\hat{H}^{(m)}t}(e^{i(k\hat{z}-(\omega+\omega_0)t)} + e^{-i(k\hat{z}-(\omega-\omega_0)t)}))e^{-\frac{i}{\hbar}\hat{H}^{(m)}t},
\end{aligned}$$

by defining $\hat{U}_0 = e^{-\frac{i}{\hbar}\hat{H}_0 t}$ and denoting the laser frequency with ω_0. Following [14], we can perform the rotating wave approximation to neglect the fast oscillating terms, $\omega + \omega_0$, as they hardly affect the time evolution of the system, and keep only the slowly varying terms, $\omega - \omega_0 = \delta$. This approximation is possible assuming that the laser is close to resonance with the ion's energy levels $\delta \ll \omega$.

We note that $e^{\frac{i}{\hbar}\hat{H}^{(m)}t}e^{ik\hat{z}}e^{-\frac{i}{\hbar}\hat{H}^{(m)}}$ is the transformation of $e^{ik\hat{z}}$ into the Heisenberg picture. In the Heisenberg picture, the position operator $\hat{z}(t)$ can be written in terms of the creation and inhalation operators,

$$\hat{z}(t) = z_0\left(\hat{a}e^{-i\omega_z t} + \hat{a}^\dagger e^{i\omega_z t}\right),$$

where $z_0 = \sqrt{\frac{\hbar}{2m\omega_z}}$ is the spread of the ground-state wavefunction. Therefore, we can write $H^{(i)}$ in the interaction picture as,

$$H_{\text{int}}(t) = \frac{\hbar}{2}\Omega_0\hat{\sigma}_+\exp\Big[i\eta(\hat{a}e^{-i\omega_z t} + \hat{a}^\dagger e^{i\omega_z t})\Big]e^{-i\delta t} + h.c.,$$

with the dimensionless parameter

$$\eta = kz_0,$$

known as the Lamb-Dicke parameter.

Working in the Lamb-Dicke regime, $z \ll \lambda \Rightarrow \eta \ll 1$, we can expand the exponents in a Taylor series and keep only terms of first order in η,

$$\hat{H}_{\mathrm{LD}} = \frac{\hbar}{2}\Omega_0\hat{\sigma}_+[1 + i\eta(\hat{a}e^{-i\omega_z t} + \hat{a}^\dagger e^{i\omega_z t})]e^{-i\delta t} + h.c..$$

The interaction Hamiltonian in the Lamb-Dicke regime, H_{LD}, consists of three terms. The carrier Hamiltonian,

$$\hat{H}_{\mathrm{car}} = \frac{\hbar}{2}\Omega_0(\hat{\sigma}_+e^{-i\delta t} + \hat{\sigma}_-e^{i\delta t}),$$

which gives rise to transitions of the type $|n\rangle|g\rangle \leftrightarrow |n\rangle|e\rangle$ with Rabi frequency Ω_0, and do not cause any change in the motional state. The red sideband Hamiltonian,

$$\hat{H}_{\mathrm{rsb}} = i\frac{\hbar}{2}\Omega_0\eta(\hat{a}\hat{\sigma}_+e^{-i(\delta+\omega_z)t} - \hat{a}^\dagger\hat{\sigma}_-e^{i(\delta+\omega_z)t}),$$

which gives rise to transitions of the type $|n\rangle|g\rangle \leftrightarrow |n-1\rangle|e\rangle$ with Rabi frequency $\Omega_0\eta\sqrt{n}$. This transition is driven by the laser when $\delta = -\omega_z$. Last, the blue side Hamiltonian,

$$\hat{H}_{\mathrm{bsb}} = -i\frac{\hbar}{2}\Omega_0\eta(\hat{a}\hat{\sigma}_-e^{i(\delta-\omega_z)t} - \hat{a}^\dagger\hat{\sigma}_+e^{-i(\delta-\omega_z)t}),$$

which gives rise to transitions of the type $|n\rangle|g\rangle \leftrightarrow |n+1\rangle|e\rangle$ with Rabi frequency $\Omega_0\eta\sqrt{n+1}$. This transition is driven by the laser when $\delta = \omega_z$. The red and blue sideband transitions entangle the internal state of the ion to its motional modes. Therefore, working in the Lamb-Dicke regime allows us to excite unique states with higher or lower motional states by simply changing the detuning of our laser.

In a Paul trap, the Lamb-Dicke parameter can be generally modified by changing V_{rf}, V_{DC}, where only V_{DC} will effect the axial Lamb-Dicke parameter,

$$\eta = k\sqrt{\frac{\hbar}{2m\omega_i}}.$$

Increasing the trapping frequencies tightens the trap, causing the ion to be more localized and the Lamb-Dicke parameter to decrease. Increasing the trapping frequencies will also shift the sidebands away from the carrier transition, allowing them to be resolved. Increasing ω_z even further will eventually make it hard to see the sidebands, as the transition will grow weak with smaller η and would require large δ, making it difficult to excite. Therefore, experimental setups would require small η that is not too small, usually aiming for $\eta \approx 0.1$.

The Ca^+ Ion

The subject of our research will be the N_2^+ molecule. Since it lacks a closed transition for laser cooling and state detection, a "logic" atomic ion will be co-trapped with it, serving as our probe. For that purpose, we will use a Ca^+ ion. Like all other alkaline earth ions, it has a single valence electron, thus a hydrogen-like energy level structure. Moreover, it has no nuclear spin ($I = 0$), simplifying its energy structure even further [20]. In addition, because the masses of Ca^+ (40 amu) and N_2^+ (28 amu) are comparable, they can be co-trapped

with ease.

In the following description of the Ca^+ energy level structure, we will use the standard notation:

$$^{2S+1}L_J.$$

Here, $L = 0, 1, 2, ...$ is the quantum number for the total orbital-angular-momentum of the electrons and is denoted by capital letters $S, P, D, ...$ The quantum number for total electron spin is S, and J is the quantum number for the total angular-momentum $J = L + S,\ L + S - 1,\ ...,\ |L - S|$.

A schema of the Ca^+ energy-level structure is shown in Figure 1 [20, 21], depicting the transitions in use and their corresponding wavelengths. Starting with a neutral calcium atom, it is being ionized via a two-photon process: first, it is excited from the ground state $^1S_0$ into $^1P_1$ by absorbing a 422 nm photon, then by absorbing a 375 nm photon the electron is excited to the continuum.

Once ionized, the Ca^+ can be trapped and manipulated in the Paul trap. The cycle used for Doppler cooling involves both the 397 nm and the 866 nm transitions. The ion is excited from its ground state $^2S_{1/2}$ into $^2P_{1/2}$ by a 397 nm photon. From $^2P_{1/2}$ the ion can spontaneously decay either back to the ground state or into the meta-stable state $^2D_{3/2}$ - both dipole allowed. Since the lifetime of $^2D_{3/2}$ is relatively long, a 866 nm laser is used to excite the ion back into $^2P_{1/2}$. Note that the absorption of a 397 nm photon, may cause an off-resonance excitation from the ground state into $^2P_{3/2}$, from which the ion may decay into another meta-stable state - $^2D_{5/2}$. Despite its low probability, the effect of this cycle is noticeable and negated by re-exciting the ion from $^2D_{5/2}$ to $^2P_{3/2}$ with 854 nm laser.

The dipole forbidden transition $^2S_{1/2} \rightarrow {}^2D_{5/2}$ induced by 729 nm laser will be used as the qubit transition. Once excited to the $^2D_{5/2}$, it can be quickly de-excited to the ground state, through the $^2P_{3/2}$, thus minimizing the duty cycle of future experiments.

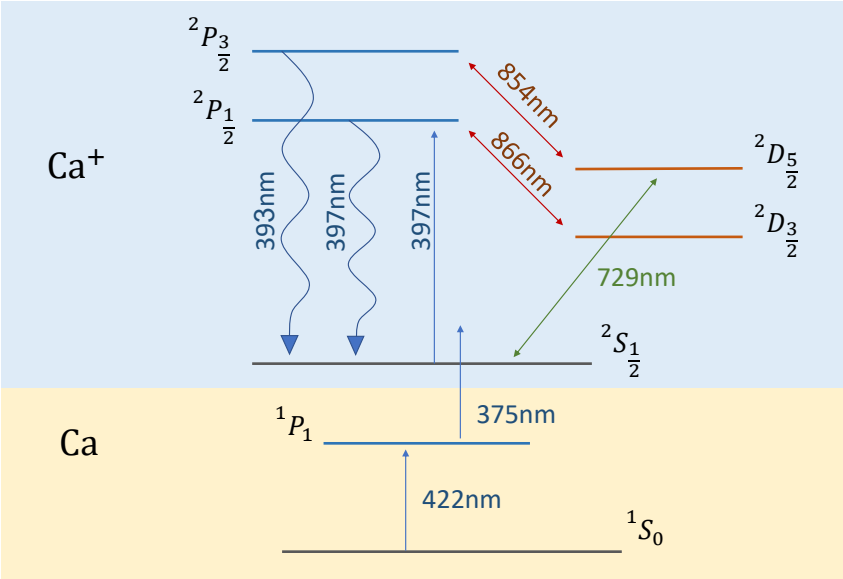

Figure 1: Scheme of Ca and $^{40}Ca^+$ energy levels used for ionization, Doppler cooling and fluorescence

Experimental Setup

The Trap

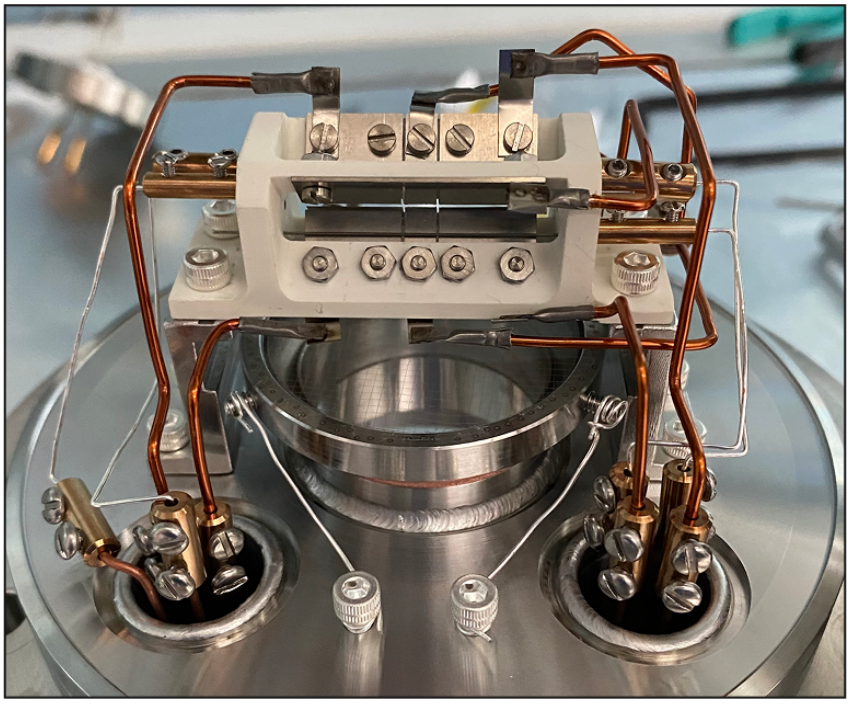

Figure 2: Picture of the ion trap

The linear Paul trap stands at the heart of the experimental setup (see Figure 2). Currently, we are using it to trap $^{40}Ca^{+}$ ions, which will be used in the future as the "logical" ions in the quantum-logic protocol. Our homemade ion trap features eight blade-shaped electrodes that generate the trapping potential, along with three rod-shaped electrodes used for micromotion compensation (MMC) and tickle, all housed in a ceramic body. A schema of the electrodes' setup is shown in Figures 3a,3b. The trap is placed in an ultra-high vacuum chamber ($P \approx 1.5 \cdot 10^{-11}$ mbar) to extend the ion's lifetime by minimizing the probability of collisions with background gas particles.

All direct current (DC) electrodes are connected to an SRS-PS350 high-voltage power supply (PS) that was set to either $V_{DC} = 40\,\mathrm{V}$ for loading ions to the trap or to $V_{DC} = 320\,\mathrm{V}$ for reaching the Lamb-Dicke regime. These voltages corresponds to axial trapping frequencies of 256 KHz and 749 KHz respectively. We note that in the theoretical description of the Paul trap, the equations are written using the angular frequencies ω_i and Ω_{rf} with units of $^{\mathrm{rad}}/_{\mathrm{sec}}$ as commonly used in the literature. Experimentally, the measured quantities are the frequencies $f_i = \frac{\omega_i}{2\pi}$, given in units of Hz. The RF voltage is induced on the RF electrodes via a helical resonator ($Q \approx 350$) for impedance matching and amplification of the 14.3 MHz RF signal. All RF signals (trapping and tickle) are generated using Quantum Machines' OPX+, which is easily controlled using Python. The OPX+ allows us to precisely control the timing of RF signals provided to various tools relative to the RF signal phase. The radial frequencies of the trap can be adjusted for various purposes by changing the output RF amplitude from the OPX+. The measured radial frequencies for a weak trap $f_l = 400\,\mathrm{KHz}$ $f_h = 622\,\mathrm{KHz}$,

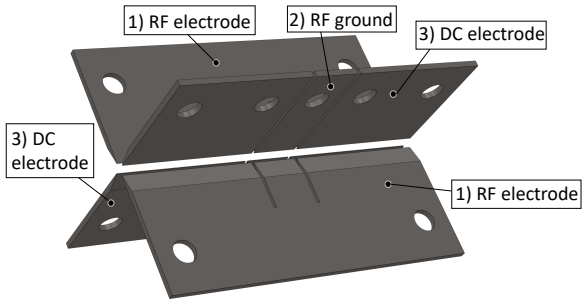

(a) The trapping electrodes

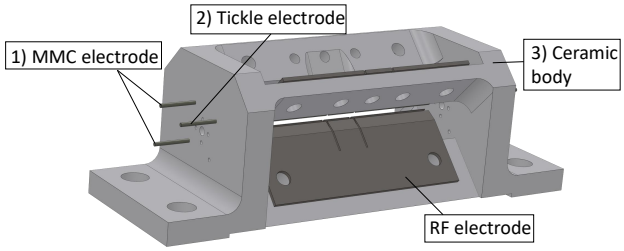

(b) Solidworks sketch of the trap

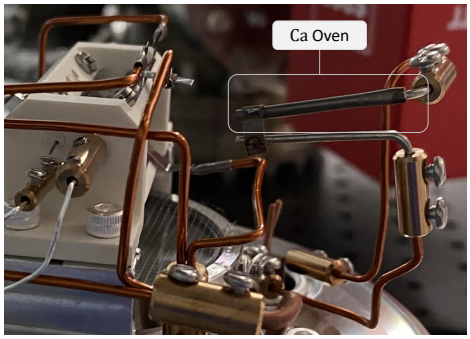

(c) Picture of the Calcium oven

Figure 3: The ion trap electrodes design. **a)** Eight blade-shaped electrodes create the trapping potential: 1) RF electrodes - induce the oscillating field in the radial axis, V_{rf}. 2) RF ground - set the reference voltage for V_{rf}. Applying a bias field, V_{b}, on the RF ground allows for the breaking of the traps' radial symmetry. 3) DC electrodes - induce the DC voltage V_{DC} which generates the axial trapping potential. **b)** Solidworks sketch of the trap and its ceramic mount in which the trapping electrodes are shown together with the three additional electrodes. 1) MMC electrodes - allow DC voltage to be applied for MMC purposes. 2) Tickle electrode - allows oscillating voltage to be applied to excite the ions' modes of motion in the trap. 3) Ceramics body - the frame to which the electrodes are screwed. **c)** Picture of the Calcium oven.

and for a tight trap $f_l = 1914\,\mathrm{KHz}$ $f_h = 2002\,\mathrm{KHz}$. In the tight trap configuration, for wavelength of 729 nm as the standard qubit transition in Calcium ions, the Lamb-Dicke parameter in the axial axis $\eta_z = 0.11$ which satisfies the Lamb-Dicke condition, and is comparable to other similar setups [3]. The bias voltage is applied through the body of the resonator using a DC PS.

The MMC electrodes are connected to a DC PS, which induces up to 25 V on each electrode. The typical MMC valuse were found to be $V_x \approx 29\,\mathrm{V}$ and $V_y = 73\,\mathrm{V}$ for $V_{DC} = 40\,\mathrm{V}$, and $V_x \approx 93\,\mathrm{V}$ and $V_y \approx 162\,\mathrm{V}$ for $V_{DC} = 320\,\mathrm{V}$. Since the compensation voltages are higher than the PS maximal voltage, an array of 9 V batteries was added on top of the PS as a steady voltage source. Since the MMC electrode circuit is open, no current is running, and the batteries are expected to be a long-lived and cheap solution. The power supply allows easy control and small adjustments, as the compensation voltages may change due to outside noise or modifications in the system.

Measuring the Trap Frequencies

The measurement of the trap frequencies is an essential step in the characterization of any ion trap. To do so, we applied an oscillatory force to the ion. Only when the oscillating force is in resonance with one of the trap modes, namely when $\omega_{\mathrm{tickle}} \approx \omega_i$, oscillation of the ion can be observed. This is called tickle. The tickle force was applied using two different methods: Amplitude modulation (AM) of the RF amplitude and through an external electrode.

Amplitude Modulation: First, we modulated the amplitude of the RF field to excite the ion's modes of motion, with modulation of the form,

$$V_{\mathrm{RF}}(t) = V_{\mathrm{rf},0}\cos\left(\Omega_{\mathrm{rf}}t\right)[1 + \beta\cos\left(\omega_{\mathrm{AM}}t\right)].$$

Here, Ω_{rf} is the trapping RF frequency, $\omega_{\mathrm{AM}} \ll \Omega_{\mathrm{rf}}$ is the modulation frequency, and β is the modulation depth. We note that there is no phase between the carrier signal $\cos(\Omega_{\mathrm{rf}}t)$ and the envelope signal $\cos\left(\omega_{\mathrm{AM}}t\right)$ thanks to the precise timing the OPX+ allows. The force applied on the ion due to the modulation is double the modulation's frequency $\omega_{\mathrm{tickle}} = 2\omega_{\mathrm{AM}}$. To understand that, let us look at the force applied to the ion

$$F = -e\nabla V_{\mathrm{lin}}\left(t\right) = -eV_{\mathrm{RF}}\left(\frac{x-y}{r_0^2}\right)\cos(\Omega_{\mathrm{rf}}t)\left(1+\beta\cos(\omega_{\mathrm{AM}}t)\right) + e\nabla\left(V_{\mathrm{DC}}(x,y,z) + V_{\mathrm{b}}(x,y)\right),$$

where V_{lin} is explicitly written in Eq. 2. The applied force consists of two terms: The first is the trapping force

$$F_{\mathrm{trapping}} = -eV_{\mathrm{RF}}\left(\frac{x-y}{r_0^2}\right)\cos(\Omega_{\mathrm{rf}}t) + e\nabla\left(V_{\mathrm{DC}} + V_{\mathrm{b}}\right),$$

which gives rise to the trapping properties of the Paul trap. The second is the tickle force, applied by the modulation

$$F_{\mathrm{AM}} = -e\beta V_{\mathrm{RF}} \left(\frac{x-y}{r_0^2}\right) \cos(\Omega_{\mathrm{rf}} t) \cos(\omega_{\mathrm{AM}} t)$$
$$= -e\beta V_{\mathrm{RF}} \left(\frac{x-y}{r_0^2}\right) \left(\cos((\Omega_{\mathrm{rf}} + \omega_{\mathrm{AM}})\, t) + \cos((\Omega_{\mathrm{rf}} - \omega_{\mathrm{AM}})\, t)\right).$$

The tickle frequency is the beating frequency of the two cos functions, which is double the modulation frequency $\omega_{\mathrm{tickle}} = 2\omega_{\mathrm{AM}}$.

This method turned out to be limited. First, for high trapping frequencies, the modulation signal decays as it passes through the helical resonator. Second, since the modulation applies only to the RF trapping field and is only in the radial plane, the excitation of the axial mode requires very high modulation depths.

External Electrode: To overcome the limitations of the AM method, we've used an external electrode (see Figure 3b) to apply the RF field for the tickle. This method is much more robust, as it is not limited by the helical resonator, and the tickle amplitude can be amplified using an external amplifier if needed. Furthermore, by using an external electrode and keeping the trapping potential constant, we ensure the dynamics of the system remain as simple as possible, eliminating the risk of observing non-linear effects, such as parametric excitation.

Loading ions

Loading a Ca^+ ion to the trap is done in a few simple steps:

1. *Heating Ca grains to create neutral Ca atoms flux.* Inside the vacuum chamber lays the calcium oven. A picture of the oven can be seen in Figure 3c. The oven is made out of a Titanium tube, 2 mm in diameter, filled with small calcium grains. Running 1.3 A current through the Titanium tube causes it to heat up, releasing Ca atoms flux directed to the center of the trap [22].

2. *Ionizing the Ca atoms via two-photon process.* Two laser beams (422 nm and 375 nm) pass through the axial axis of the trap, ionizing the neutral Ca atoms according to the scheme presented in Figure 1.

3. *Cooling the ions using Doppler cooling.* 397 nm and 866 nm laser beams pass through the center of the trap at an angle of 45° to the axial axis with equal projections on both radial axes. This allows for Doppler cooling both in the axial and radial axes. These lasers scatter photons on a closed cycle transition in the ion (see Figure 1), causing it to fluoresce, thus enabling us to detect the ion using an imaging setup and a CCD camera, much like Figure 4.

4. *Reduction of excess ions.* In case multiple ions were trapped, turning the RF voltage off for a short duration may eject some ions while keeping others trapped. The required duration depends on the trap depth, the number of trapped ions, and the quality of the MMC. The dynamics of this ion reduction process and the role of these factors are not yet fully understood. Further study of this process will be beneficial for future experiments and may reveal unknown features of Paul traps.

Executed properly, these steps allow trapping a single Ca^+ ion within $\sim 5\,\text{min}$. Most of the time is spent waiting for the oven to heat up from room temperature. Since we have only a single oven in the vacuum chamber, we take precautionary measures, such as limiting the current running through the oven and implementing an external timer that limits the oven operation to 10 minutes. The second most time-consuming step is the reduction step. However, after some experimental trial and error, one can perform this task relatively fast (below 1 minute). The typical lifetime of a trapped ion is $\sim 1\,\text{day}$

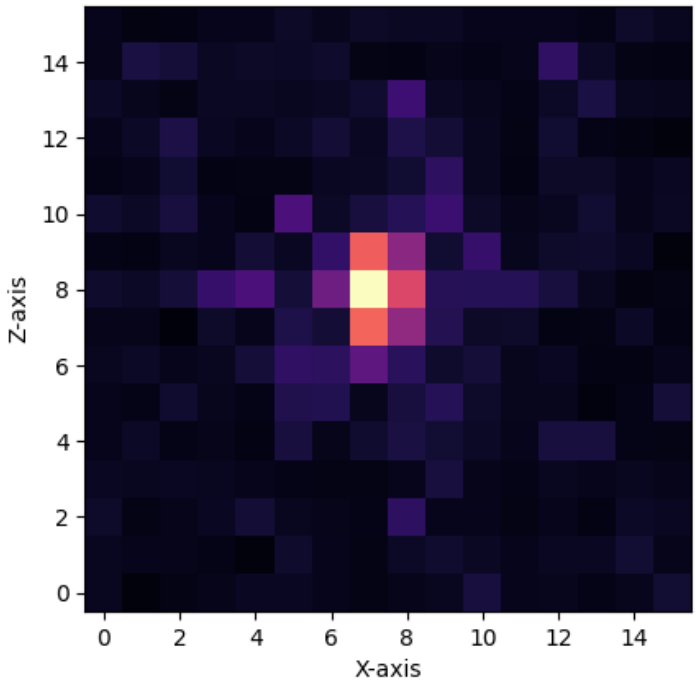

Figure 4: Photo of a single trapped ion

Optical Setup

Second only to the Pual trap, lasers serve as our primary instrument for the control and manipulation of ions. Currently, our optical setup enables the ionization, cooling, and detection of calcium ions. In the future, we plan to implement additional laser lines to achieve coherent quantum control over the charged atom-molecule pair, enhance cooling to reach the motional ground state, and incorporate additional MMC methods. The design of the optical setup integrated into the trap is illustrated in Figure 5. The output wavelengths are written in nm next to their corresponding collimators. Wavelengths written in black correspond to operating laser lines, while orange labels represent laser lines that have not been implemented yet.

All Ca-related laser beams in use are produced using commercial lasers (Toptica DL PRO) and placed in a designated laser room (with the exception of the 375 nm laser, which is a Toptica iBeam-smart model and is located next to the ion trap setup). In the laser room, a small percentage of the laser power is collected into HighFinesse WS8-10-VIS wavemeter, which is used to lock and control the lasers. All beams are transported to the main experiment via optical fibers.

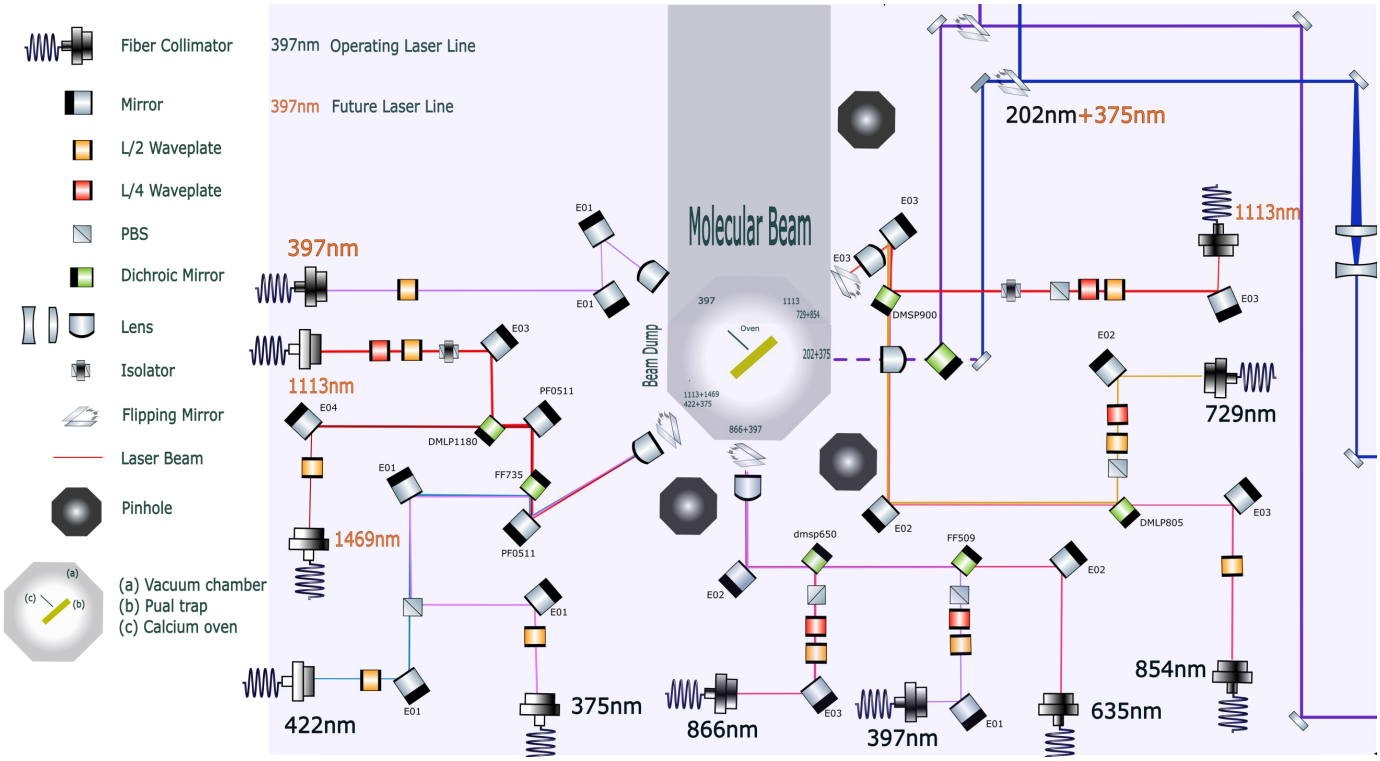

Figure 5: Optics design around the ion trap's vacuum chamber. The wavelength of each laser is stated in nm next to its corresponding input collimator. The wavelengths of laser lines in use are written in **black**, and the wavelengths of future lines are written in **Orange**. Each laser beam was assigned a distinct color for clarity. The 422 nm and 375 nm lasers ionize the calcium atoms. The 397 nm and 866 nm are used for Doppler cooling and combined with the 854 nm laser, enable continuous fluorescence of the Ca^+ ions. Due to the wide range of wavelengths, the models of each mirror and filter are stated next to it, corresponding to Thorlabs and Semrock catalogs. Waveplates and polarizing beam splitters (PBSs) allow control over the light's polarization. The flipping mirrors are usually open, allowing the light to enter the trap. In case re-alignment of the beam is necessary, the flipping mirror can be shut closed, reflecting the light into a designated pinhole that acts as a reference point.

The present setup consists of two groups of lasers, each with a different function:

- *Ionization* - The natural calcium atoms are ionized via $1+1'$ resonance-enhanced-ionization scheme. The 422 nm laser excites the atoms into a high electronic state, and the 375 nm laser excites the electron into continuum [23]. By tuning the wavelength of the 422 nm laser, we can selectively ionize the desired Ca isotope [22]. The beams' optical path prior to the trap is used to create an overlap between the beams, increasing the efficiency of the process. The lasers propagate along the axial axis of the trap orthogonal to the oven's flux direction, thus, minimizing Doppler shifts in the ionization process.

- *Cooling and fluorescence* - In Doppler cooling, an atom is exposed to a laser beam that is slightly red-detuned from an atomic transition. As the atom moves antiparallel to the propagation of light, the laser is blue-shifted relative to the atom due to the Doppler effect, shifting the laser closer to resonance. Atoms that are moving parallel to the propagation of light, shift the laser away from

resonance. Therefore, atoms that are moving opposite to the k vector of the laser are more likely to be excited. Upon excitation, the atom absorbs the photon, receiving its momentum. Since the photon usually carries momentum with an opposite sign to the atom, this absorption results in the deceleration of the atom. As the atom de-excites, it releases a photon in a random direction. Over many excitation cycles, this effect cancels out, and the atom is being cooled [24].

In our system we use the $^2S_{1/2} \rightarrow {}^2P_{1/2}$ transition for the Doppler cooling, induced by the 397 nm laser and by the 866 nm laser as a repump (see Figure 1). The full description of the Doppler cooling cycle is given in the section regarding the Ca^+ energy level structure. The 397 nm wavelength photons that were scattered as a by-product of the Doppler cooling are collected into a CCD camera for detection of the ion. Usually, one laser beam can Doppler cool only one axis of motion. Here, the ion's motion is dictated by the Paul trap; hence, cooling can be done using only one beam that is not perpendicular to any modes of motion in the trap. We note that this is only possible when the degeneracy of the radial trapping frequencies is lifted. In the degenerate case ($b_i = 0$ Eq. 3), the ion's momentum perpendicular to the laser beam remains unchanged as there is no energetically preferred axis for its motion.

Three additional laser systems will be implemented in our setup, enabling coherent quantum control over the Ca^+ and N_2^+, which are not part of the work described in this thesis:

- *Ca^+ qubit transition* - The two energy states we will use as the Ca^+ qubit states are its ground state $^2S_{1/2}$ and the metastable state $^2D_{5/2}$. The qubit transition will be induced by the 729 nm laser beam, and the 854 nm will allow fast quench from $^2D_{5/2}$ to the ground state through a third, unstable, energy level ($^2P_{3/2}$). Both lasers are aligned with the trap's axial axis, since we wish to couple the internal state of the trapped ions only to the axial modes of motion.

- *N_2 Ionization* - The molecular-beam machine produces a flux of internally cold, neutral N_2 molecules into the trap's vacuum chamber. Then, the molecules are ionized by the 202 nm and 375 nm lasers in a 2+1' ionization process. These laser beams enter the trap perpendicular to the molecular flux to minimize Doppler shifts in the ionization process, similar to the Ca ionization.

- *N_2^+ state detection and coherent control* - Once the Ca^+ and N_2^+ ions are co-trapped, their common modes of motion must be coupled to the N_2^+ internal state to enable state detection and coherent control. We will use the 1113 nm and 1469 nm laser lines to apply a state-dependent force on the N_2^+ ion, which will realize this coupling. Once again, we will align the lasers along the trap's axial axis, as we wish to utilize only motional modes in this axis.

Results

Trapping Frequencies

In this project, we've characterized the trapping frequencies as a function of the various trapping parameters: V_{rf}, V_{DC}, V_{b}, Ω_{rf}, starting from a shallow trap and moving up to a tight trap which is in the Lamb-Dicke regime. The frequencies were measured using tickle, induced either by modulating the RF field amplitude or by applying an external field. For every set of trapping parameters, we've scanned the tickle frequency, $f_{\mathrm{tickle}} = \omega_{\mathrm{tickle}}/2\pi$, and measured the ion's response. Significant response was measured when the tickle frequency matched one of the trapping frequencies (see Figure 6a and 6b), and no response was measured otherwise. The results from one f_{tickle} scan are shown in Figure 7.

For each tickle frequency, a picture of the ion was taken using our imaging system, with an exposure time of $\sim 0.5\,\mathrm{sec}$. According to [25], the intensity profile of a 1D oscillating ion is

$$I(x) = \int_0^{2\pi} I_0 \exp\left\{[-\frac{(x - x_0 - A\cos(\omega_{\mathrm{tickle}}t))^2}{2\sigma^2}]dt\right\} + B_g. \tag{5}$$

This function describes the ion's intensity profile as a Gaussian with intensity amplitude I_0, center position x_0, and standard deviation (std) σ, which oscillates with amplitude A and frequency ω_{tickle} - the tickle frequency. The background intensity is denoted by B_g. During the measurement, the oscillations are averaged over, as the camera exposure time is much longer than the cycle time of the oscillations.

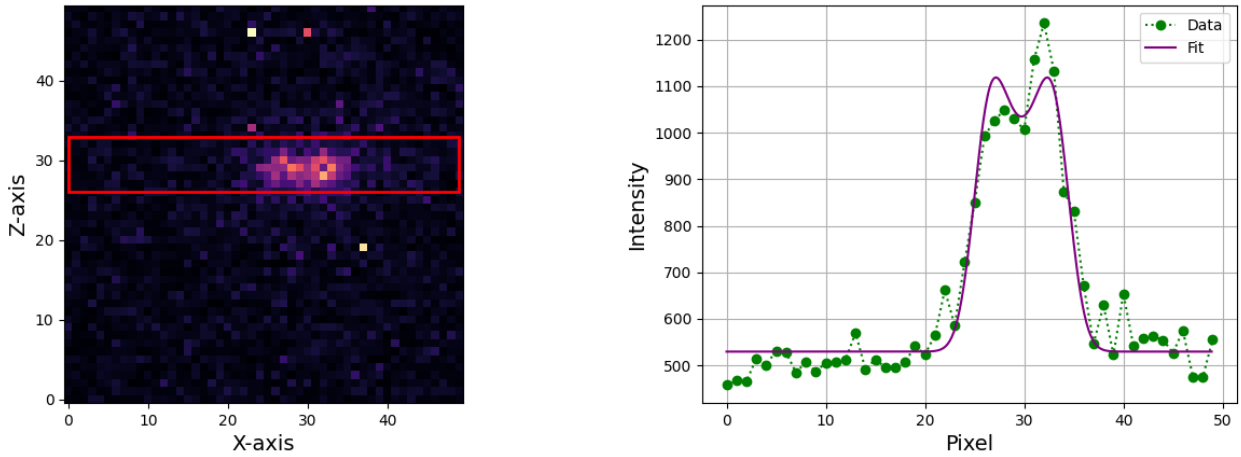

(a) (b)

Figure 6: Tickle measurement for $\omega_{\mathrm{tickle}} \approx \omega_{-}$. **(a)** Picture of an ion oscillating in the low radial mode. The red rectangle marks the area used to calculate the 1D intensity profile. **(b)** The ion's average intensity along the picture's x axis (green circles). The 1D intensity profile was fitted to 5 (purple line) to determine the response amplitude of the ion.

Our imaging system aligns with the axial mode of the trap (Z-axis in Figure 6a) and a projection of the two radial modes of the trap (X-axis in Figure 6a). For that, oscillations in all three modes can be seen on

the 2D image - axial oscillations along the Z-axis and both radial oscillations along the X-axis of our imaging system (Figure 6a). To obtain a quantitative measure of the ion's response, the ion's 1D intensity profile was calculated for each picture, according to the measured mode. To do so, the pictures were first sliced in the adjacency of the ion, perpendicular to the measured mode (Z-axis in Figure 6a for radial oscillations and X-axis in Figure 6a for axial oscillations) and then averaged along the complementary axis (X-axis in Figure 6a for radial oscillations and Z-axis in Figure 6a for axial oscillations). Once calculated, the 1D intensity profile was fitted to Eq. 5, as shown in Figure 6b. As the ion oscillates, its amplitude along the image plane grows, thus A increases. In addition, oscillations in the radial modes involve motion in and out of the imaging plane, which causes the focusing and de-focusing of the ions image, increasing σ. Therefore the ion's response amplitude was defined as $\sqrt{\sigma^2 + A^2}$. The ion's std and oscillation amplitude were calculated using the fit, and the trapping frequencies were found by looking for their maximal values (Figure 7).

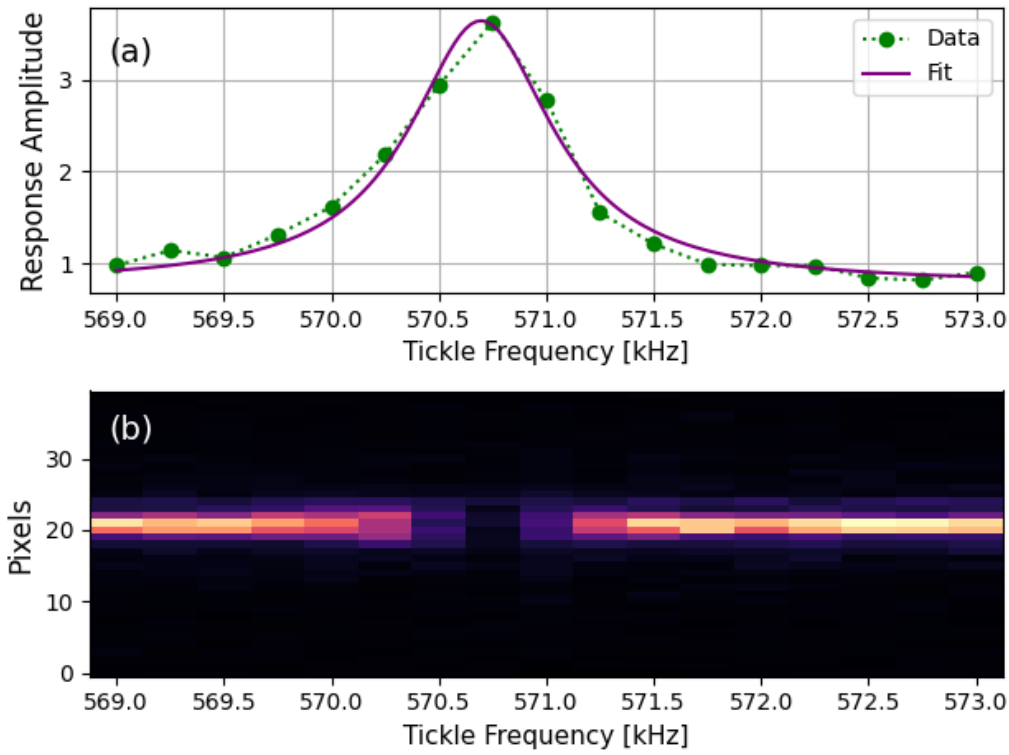

Figure 7: Scan of the low radial mode of a trapped ion using tickle. **(a)** Plot of the ion's response as a function of the tickle frequency. The measured data (green dots) was fitted to a Lorentzian (purple line) to interpolate the location of the maximal response, which corresponds to the low radial trapping frequency. In this section, the resonance frequency values were extracted "by eye". In the next section, where we discuss the stability of the radial frequencies, we utilized the enhanced precision enabled by the fit. **(b)** Heat map of the 1D averaged ion intensity (Fig. 6a) for different tickle frequencies.

The measured trapping frequencies at various DC voltages were plotted in Figure 8 and compared with the theory. Starting from $V_{\mathrm{DC}} = 40\,\mathrm{V}$, the axial trapping frequency is low $\omega_z/2\pi = 256\,\mathrm{kHz}$ and $\eta_z \approx 0.2$. As we increase V_{DC}, the trap becomes tighter until the Lamb-Dike condition is satisfied with $\eta_z \approx 0.11$ and

$\omega_z/2\pi = 716\,\mathrm{kHz}$. For each data point, optimal parameters were found for the MMC and laser cooling. The MMC parameters showed high dependence on the DC voltage, meaning that the DC electrodes are the main source of drift voltage, which shifts the trapped ions from the center of the trap.

The theoretical values were extrapolated from a single data point, according to Eq. 3. We note that direct calculation of a, b, and q cannot be done since r_0 and z_0 are unknown, as (r_0, z_0) are not the dimensions of our linear trap but that of an ideal trap with hyperbolic-shaped electrodes. Therefore we've calculated a_{ref} using a reference axial frequency that was measured in a reference voltage $V_{\mathrm{DC}}^{\mathrm{ref}}$ and used it to calculate $\frac{1}{2}q_{\mathrm{ref}}^2 \pm b_{\mathrm{ref}}$ at a reference radial frequency $\omega_{\pm}^{\mathrm{ref}}$. The frequency can then be calculated by scaling up a_{ref} proportionally to V_{DC} according to Eq. 1. This naive extrapolation is plotted as the yellow curves in Figure 8. Clearly, there is a mismatch between the naive extrapolation and the measured values. Therefore, we've taken a phenomenological approach in order to adjust the ideal theory to our experimental setup. The results of the modified extrapolation are plotted as the purple curve, showing good agreement with the measurements. In the following, we will explain this phenomenological approach we have taken.

Recall that the potential of the linear Pual trap (Eq. 2) is true for the ideal case of perfectly symmetric quadrupoles, in which both V_{rf}, V_{b} are symmetric to infinite translations in the Z-axis, and V_{DC} has perfect radial symmetry. In our trap, both symmetries are slightly broken: the first due to the finite size of the trap, and the second because the DC electrodes are placed in the (y, z) plane (see Figure 3a), distinguishing the X and Y axes. Therefore, the general potential of the realistic Paul trap will be of the form

$$V_{\mathrm{lin}}^{\mathrm{gen}} = \frac{1}{2}V_{\mathrm{rf}}(t)\left(1 + \frac{(1+\alpha)x^2 - (1-\alpha)y^2 - 2\alpha z^2}{r_0^2}\right) - \frac{1}{2}V_{\mathrm{DC}}\frac{(1+\varepsilon)x^2 + (1-\varepsilon)y^2 - 2z^2}{z_0^2} - \frac{1}{2}V_{\mathrm{b}}\frac{(1+\beta)x^2 - (1-\beta)y^2 - 2\beta z^2}{r_0^2}.$$

With α, β, ε asymmetry factors. This form can be further simplified using two assumptions. First, since both the DC electrodes and the RF ground electrodes (V_{b}) lie in the same plane and are subject to the same geometry, we assume $\beta = \varepsilon$, meaning that both quadrupoles experience the same symmetry-breaking factor. Second, as the RF electrodes (V_{rf}) are longer than the RF ground electrodes (V_{b}) by approximately an order of magnitude, reducing the effect of the translational symmetry breaking, we assume $\alpha = 0$. Hence the realistic potential of our trap is

$$V_{\mathrm{lin}}^{\mathrm{real}} = \frac{1}{2}V_{\mathrm{rf}}(t)\left(1 + \frac{x^2 - y^2}{r_0^2}\right) - \frac{1}{2}V_{\mathrm{DC}}\frac{(1+\varepsilon)x^2 + (1-\varepsilon)y^2 - 2z^2}{z_0^2} - \frac{1}{2}V_{\mathrm{b}}\frac{(1+\varepsilon)x^2 - (1-\varepsilon)y^2 - 2\varepsilon z^2}{r_0^2},$$

with the modified dimensionless parameters:

$$q_i = [q,\, -q,\, 0],\; a_i = [-(1+\varepsilon)a,\, -(1-\varepsilon)a,\, 2a],\; b_i = [-(1+\varepsilon)b,\, (1-\varepsilon)b,\, 2\varepsilon b]. \tag{6}$$

As before, the trapping frequencies are calculated according to Eq. 3, using the modified parameters. Extrapolating for the asymmetric case, we've managed to measure asymmetry factor

$$\varepsilon \approx 0.135.$$

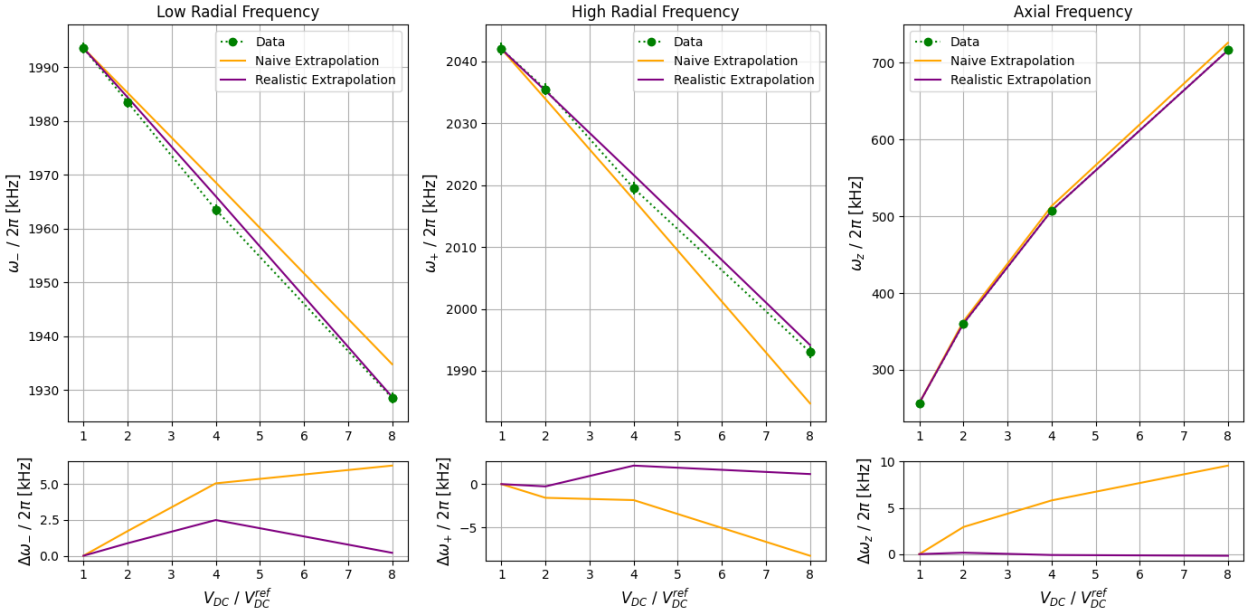

Figure 8: Trapping frequencies as function of $V_{\mathrm{DC}}/V_{\mathrm{DC}}^{\mathrm{ref}}$. In each figure, the measured values are plotted (green circles), and compared to both naive (yellow line) and realistic (purple line) extrapolations. The difference between the extrapolations and the measured values ($\Delta\omega_i$) is plotted under each figure, using the corresponding color. Acknowledging that the trap's structure induces small symmetry breaking in V_{DC} and V_{b} allows for more accurate extrapolations. We note that the measured radial frequencies in $V_{\mathrm{DC}}/V_{\mathrm{DC}}^{\mathrm{ref}} = 4$ are lower than the realistic extrapolation prediction. This may be caused by fluctuations in the resonator output power, affecting both radial frequencies in the same manner.

In the same manner, the trapping frequencies were measured and extrapolated using both symmetric and asymmetric potentials for different input RF amplitudes, as shown in Figure 9. The axial trapping frequency measurement (right plot) shows that it is independent of the RF voltage, as both naive and realistic models predict. This result confirms our prior assumption that the RF quadrupole in our trap can be treated as symmetric.

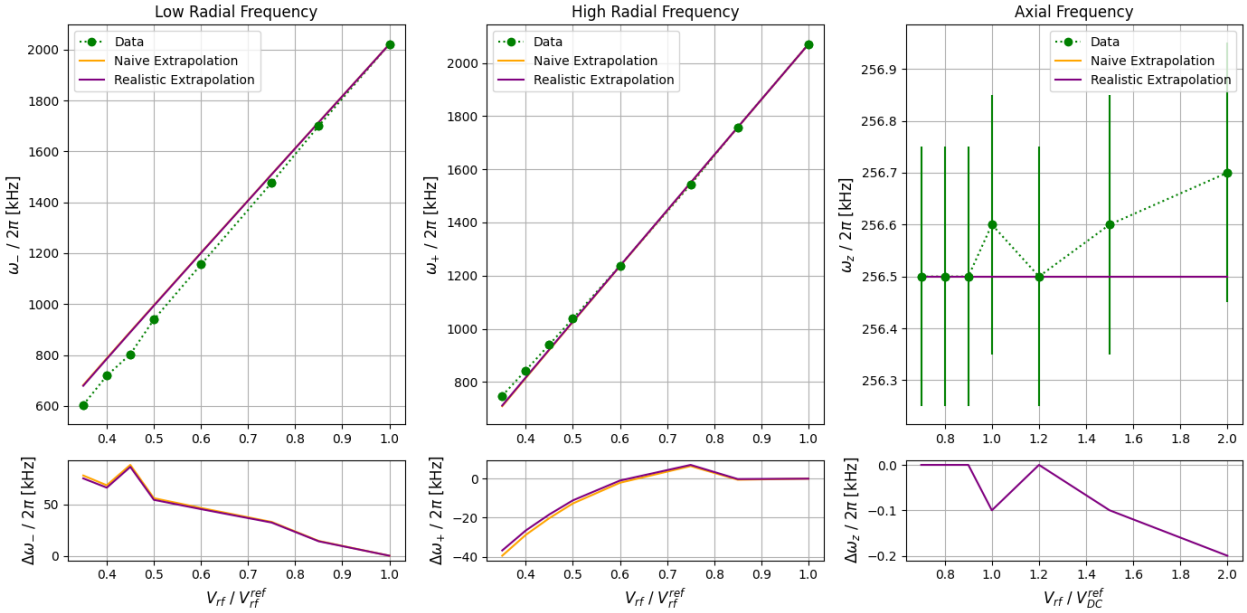

Figure 9: Trapping frequencies as function of $V_{\mathrm{rf}}/V_{\mathrm{rf}}^{\mathrm{ref}}$. In each figure, the measured values are plotted (dotted green curve), and both naive (yellow curve) and realistic (purple curve) extrapolations. The difference between the extrapolations and the measured values ($\Delta\omega$) is plotted under each figure, using the corresponding color. The axial frequency (right plot) does not change with V_{rf}, verifying that $q_z = 0$. The extrapolation for both radial frequencies fails to predict the measured values, expecting ω_- (ω_+) to be higher (lower) than measured, for small values of $V_{\mathrm{rf}}/V_{\mathrm{rf}}^{\mathrm{ref}}$, meaning that q is smaller than expected relative to b.

In the radial frequency case, both extrapolation methods fail to calculate the measured values. Choosing the highest RF input voltage as the extrapolation reference point, we observe that as V_{rf} decreases, the difference between the two radial modes, $\Delta\omega_{\pm} = \omega_+ - \omega_-$, increases faster than predicted. This indicates that the measured values of q decrease more quickly, making the effect of b more significant. It is worth noting that the linear dependence of the RF trapping amplitude on the input RF amplitude has been measured and verified.

This unexpected behavior of the radial frequencies, influenced by the interplay between q and b, becomes even more evident when measuring $\omega_{\pm}$ dependence in V_{b}. As seen in Figure 10, the radial frequencies follow an "avoided-crossing" behavior, suggesting a coupling between q and b. An experimental study of this phenomenon was recently done by R. Saito [26], showing that structural asymmetries in the trap may cause this avoided-crossing behavior and that by changing V_{b} the principle axes of the trap can be rotated. Using the asymmetric model (Eq. 6) to calculate the radial frequencies in our trap, we see that asymmetry alone cannot explain the observed avoided-crossing, as it predicts the existence of b for which $\omega_+ = \omega_-$. An ongoing work in our group, done together with Tali Shemma, suggests that only when the bias quadrupole (V_{b}) is rotated relative to the RF quadrupole (V_{rf}), asymmetric traps will experience coupling between b and q that will lead to the avoided crossing.

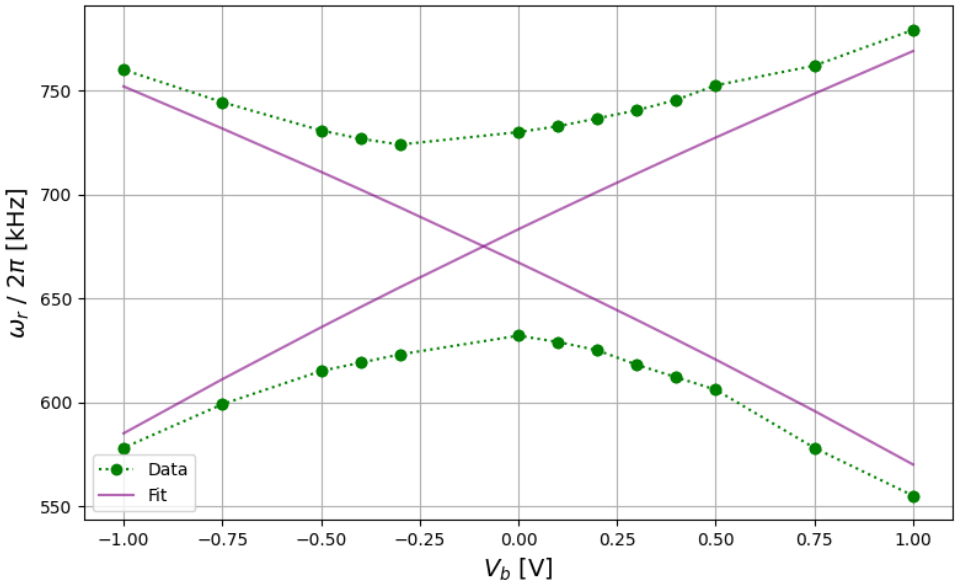

Figure 10: Radial trapping frequencies as function of V_b. The measured values (green dotted lines) follow an unexpected avoided-crossing behavior, implying coupling between q and b. By plotting an illustration of the expected measurement outcome (purple solid lines), we see that the asymmetry of the trap shifts the crossing point from zero to $V_\mathrm{b} = -0.13\,\mathrm{V}$, but cannot explain the avoided-crossing. To plot the illustration, data points for large V_b values were estimated and assigned to each curve based on the expected outcome of the measurements before fitting to Eq. 3.

Comparing the results of measuring $\omega_\pm$ as a function of V_rf and V_b, we observe that in both cases, the difference between the two radial frequencies is greater than expected. The gap between ω_+ and ω_- is governed by the interplay between q and b; hence, we assume that the effect of the proposed coupling between q and b appears in both measurements. Further theoretical work is required to develop a mathematical model that incorporates this coupling and verify our assumptions.

Lastly, the trap's dependence on Ω_rf had to be studied to obtain a complete picture of our parameter space. Recall that a helical resonator amplifies the RF voltage and serves as an impedance-matching element between the OPX+ (RF source) and the RF electrodes. Small deviations from the resonator's center frequency will cause a dramatic decrease in the transmitted RF power, hence smaller RF voltage on the electrodes. Therefore, the values of Ω_rf are constrained by the resonator.

Taking this constraint into account, we measured the low radial frequency ω_- (green circles), the transmitted RF power (red line), and the reflected RF power (pink line), as a function of small changes in the RF frequency, starting from the point of minimal reflections (see Figure 11). The maximum value of ω_- is reached at the same Ω_rf as the peak transmitted power, in which the RF amplitude on the electrodes is indeed maximal. Identifying this value is crucial for future experimental work, as it corresponds to the point where the radial frequencies are least sensitive to variations in Ω_rf, satisfying $\dfrac{\partial\omega_\pm}{\partial\Omega_\mathrm{rf}} = 0$. This makes it a favorable operating point, since variations in Ω_rf are equivalent to variations in the resonator's center frequency. As discussed in the next section, the resonator is a primary source of noise in our system. It is interesting to note that the maximal transmission and minimal reflection points do not overlap.

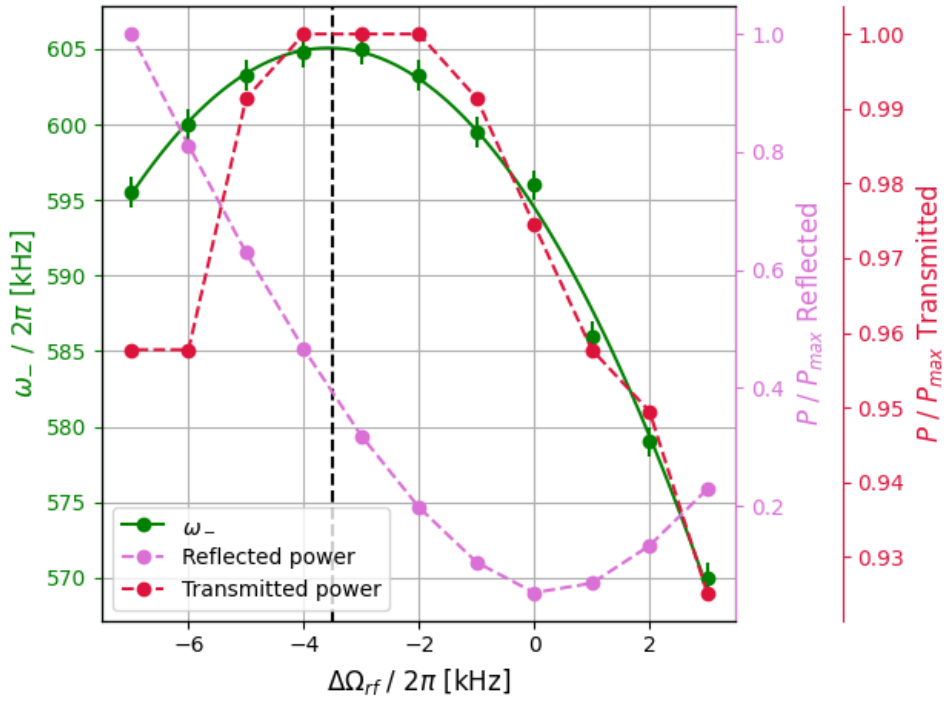

Figure 11: The effect of small changes in Ω_{rf} relative to the minimal reflection point on the following: Low radial frequency - data as green circles and quadratic fit as green line, RF reflected power - pink dashed line, and transmitted power - red dashed line. The values of $\omega_-/2\pi$ are plotted on the left Y-axis, while the transmitted power is plotted on the right-most Y-axis, and the reflected power is plotted on the middle-right Y-axis. The power values are normalized to their respective maximum measured values for clarity. The maximum of ω_- was extracted using a quadratic fit and occurs at $\Delta\Omega_{\text{rf}} = -3.5\,\text{kHz}$. This maxima agrees well with the point of maximum transmitted power as compared to the clear deviation from the point of minimal reflections.

Radial frequencies stability

During our daily experimental work, we observed significant drifts in the radial frequency values for a fixed set of trapping parameters, making it difficult to compare measurements taken on different days and introducing noise into long-duration measurements. After investigating the issue, we identified that the cause of this instability was the helical resonator, which induces the RF voltage on the trap's electrodes. To verify this, we measured both the output power of the resonator and one of the radial frequencies over several hours. As shown in Figure 12a, the drift in frequency and transmitted RF power follow the same trend. By plotting the normalized frequency against the normalized power, in Figure 12b, their correlation becomes evident. This correlation remains consistent across measurements taken over three days, as shown in Figure 12c.

This insight led us to implement an RF lock - a digital PID mechanism that locks the RF power at a constant value by adjusting the input voltage. The RF lock runs on the lab PC via a Python script, which reads the RF power every 1 sec and adjusts the voltage output of the OPX+. By default, the OPX+ outputs RF pulse signals, limited to pulse length of $\sim 65.5\,\mu$sec. Therefore, the trapping RF signal was defined as a "sticky" element - an internal definition of the OPX+. "Sticky" elements allow for the generation of

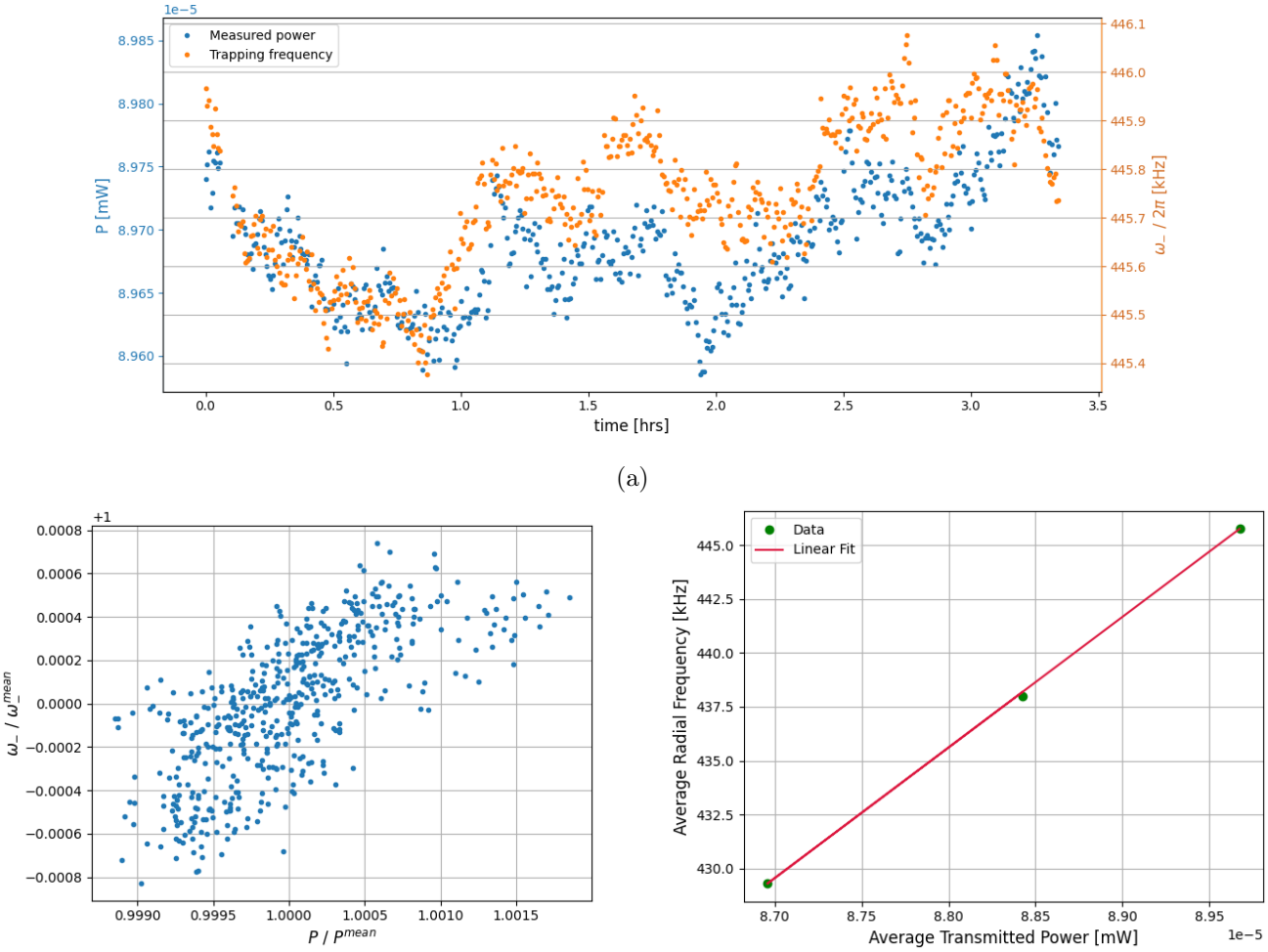

Figure 12: Correlation between the radial frequencies and transmitted RF power. **(a)** Measuring the values of the RF power (orange dots, left Y-axis) and low radial frequency (blue dots, right Y-axis) over the course of three hours shows that both follow the same trends. **(b)** Normalized ω_- against the Normalized RF power showing the correlation between the two parameters. **(C)** Daily averaged ω_- against the transmitted power, as measured on three consecutive days (green dots) and their linear fit (red line), showing that the correlation between the radial frequency and the power is consistent.

continuous signals and for online adjustments of its amplitude and frequency. With this, digital RF power locking became possible in principle.

However, any change to the amplitude of a "sticky" element is represented in the OPX+ by a float with a resolution of 16 bits, such that the RF amplitude is discretized. This discretizations cause a discrepancy between the actual RF amplitude and the variable for the RF amplitude in the lab PC. This is because the amplitude of "sticky" elements can be modified only through adding or subtracting from their current amplitude. Thus, the value of the RF amplitude is modified differently in lab PC and in the OPX+. This discrepancy grows with every adjustment done in the locking procedure, making the RF lock unusable within about an hour.

This issue can be solved by synchronizing the lab PC and the OPX+ regularly, which involves restarting the phase or the amplitude of the RF signal; both cause abrupt changes in the RF signal. Wise integration of these solutions may allow their implementation such that the precision of our future measurements will not be affected. For example, restarting the input RF amplitude faster than the resonator's response may not affect the trapping RF amplitude, provided that the signal's phase remains unchanged. Another solution is to match the resolution of the lab PC to that of the OPX+, which requires a better understanding of the OPX+ float to binary mapping.

Although the RF locking mechanism is not fully operational yet, the progress made so far has been valuable and it was used, e.g, in [27], to better control and adjust the radial trapping frequencies. "Sticky" elements are a central tool in our lab as the majority of RF signals (including the Paul trap and AOMs) are controlled in this manner. Gaining a better understanding of them is beneficial for our future work.

Moving to the new Lab

Pioneering scientific work, as we're aiming to achieve, must begin in known and familiar realms. In our case, these realms were the mostly unused labs of existing groups in our department, leading to our setup being split between two rooms — the ion trap in one and the molecular-beam machine in the other. In this temporary state, the majority of the experimental setup was constructed and tested, and the group's first ions were trapped. However, the transition to the permanent lab needed to be carefully planned, along with the required upgrades for integrating the ion trap with the molecular-beam machine and future laser lines. Here, we describe the design of the ion trap table and breadboard, which facilitates the optical setup.

When designing the table for the trap's vacuum chamber, we had to account for a few constraints imposed by the molecular beam machine's design. First, the height of the trap's vacuum chamber had to match that of the molecular beam machine to ensure proper connection between the two setups. In addition, since the molecular beam machine was mounted on a designated rack to facilitate its transport between the temporary and permanent labs, the trap's vacuum chamber must remain fixed relative to it. This ensures that the molecular beam stays aligned and prevents structural damage, meaning that active vibration damping cannot be used. Therefore, we chose a rigid table frame (27.5" high) and placed a "Nexus" honeycomb breadboard (4.3" high) on top of it, to maximize the vibration damping while ensuring the total height does not exceed that of the molecular beam machine.

Due to the vacuum chamber, the trap is elevated by 10" above the optical table. Therefore, all incoming

laser beams must match this height, requiring the necessary optical elements to be raised accordingly. Looking at Figure 5, one can see that many optical elements are required. As a result, a large breadboard is preferred to fit the current design while leaving room for additional unplanned optical lines if needed. However, increasing the size of the breadboard makes it harder to lift and support.

The final design is presented in Figure 13. We are using two 24"×36"×0.75" solid aluminum breadboards, which were cut to fit tightly around the trap's vacuum chamber. Using two breadboards allowed for easy assembly and for custom adjustments made by the department's workshop. Each breadboard is supported by eight posts, each with a 1.5" diameter and a height of 8". The posts are screwed to the optical table below with four screws via PB1 pedestal [1], providing greater resistance to torque compared to the standard clamping fork. The breadboards are attached to the posts using clamping forks screwed to their underside, allowing for quick assembly and disassembly. Finally, unique pins placed on three of the posts of each breadboard (highlighted in red) define the exact position of the breadboards, ensuring that temporary removing them for maintenance will not cause significant misalignment in the optics. Notably, in the optical configuration design (Figure 5), the laser lines do not cross from one breadboard to the other, minimizing the impact of potential drift or relative vibrations.

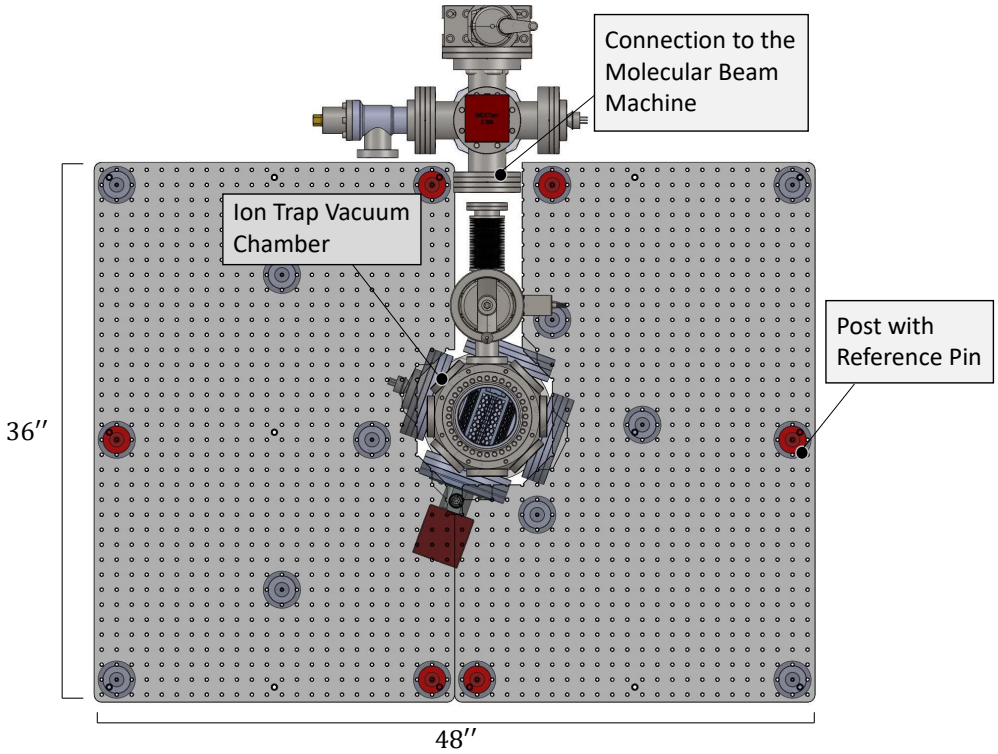

Figure 13: Design of the breadboards around the trap.

[1] PB1 in Thorlabs catalog

Once the transition to the permanent lab was completed, the optical setup had to be assembled and aligned to re-trap ions. The minimal requirement for re-trapping ions is functional and well-aligned trapping, ionization, cooling, and imaging systems. Since these setups had already been tested and used to trap ions in the temporary lab, only re-alignment was necessary. The main challenge in the alignment was estimating the ions' position in the trap and initially having to direct the laser beams and imaging system blindly. To do so, a different approach was taken for each system.

In the ionization setup, the 375 nm and 422 nm laser beams propagate along the axial axis of the trap, according to Figure 5. The trap's ceramic frame (Figure 3b) features two designated holes along the axial axis, allowing the laser beams to enter and exit the trap. Maximizing the laser beams' power at the far side of the trap ensures proper alignment.

Using the trap's electrodes as a reference, the imaging system can be directed to the center of the trap, providing a reasonable estimate of the ion's position. However, this process is not straightforward, as the imaging system's field of view cannot capture all six trapping electrodes in a single frame (see Figure 3a). Therefore, we used the translational mount of the imaging system to shift its position until we observed the gap between the DC electrode and the RF ground electrode, as shown in Figure 14a. We then moved the imaging system along the electrode to locate the opposite gap between the RF ground and the second DC electrode. By measuring the translation required to shift from one gap to the other, we estimated the center of the trap as the midpoint of this translation. This procedure was repeated for each axis, using the relevant electrodes as reference points. When aligning the imaging system, it is important to maximize its field of view, use minimal gain to prevent potential damage, and adjust the 397 nm laser such that its scattering from the electrodes is visible but not blinding.

The cooling setup is the most difficult to align, as it requires the highest accuracy but lacks clear reference points. A rough alignment to the trap's center can be done by minimizing the 397 nm scatter from the electrodes. Fine alignment, however, is performed using the ions as a reference. Therefore, a large number of ions are trapped, creating a spread-out cloud that increases their cross-section with the laser beams. A mirror, common for 397 nm and 866 nm laser beams, is then used to scan their intersection with the trap. The initial alignment is complete once the ion cloud is observed, similar to the image in Figure 14b.

Once ions are observed, fine-tuning can be done to optimize the alignment.

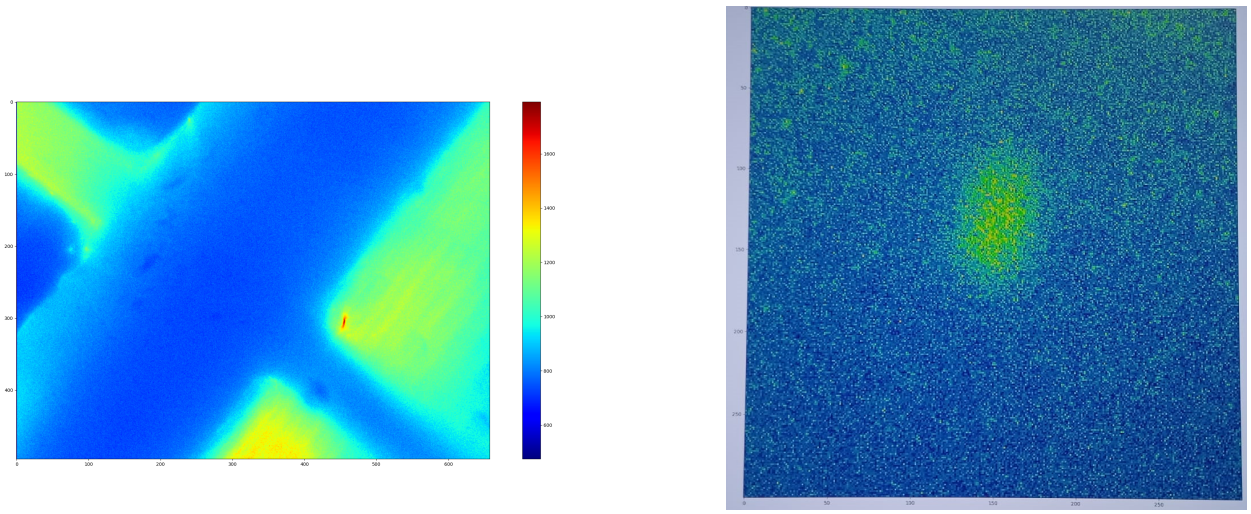

(a) (b)

Figure 14: Images from the ions' re-trapping in our permanent lab. **a)** The gap between the RF ground electrode and one of the DC electrodes (Figure 3a), as seen in our imaging system. **b)** A picture of the first trapped ions' cloud in our permanent lab. By trapping a large number of ions, we increase their cross-section, thus simplifying the alignment process.

Discussion

In this thesis, we mapped the parameter space of a linear Paul trap and identified the optimal operational values for various applications, ranging from ion trapping to precise quantum control. To do so, we implemented two methods for performing tickle measurements: modulation of the trapping RF field's amplitude and application of an external RF field induced by a designated electrode. The latter was found to be the preferred approach. We upgraded the 397 nm and 866 nm laser lines, enabling precise control of the laser cooling parameters and identifying values that ensure robust cooling across different trapping frequencies. The tickle measurements confirmed that our ion trap can be tuned to the Lamb-Dicke regime with $\eta \approx 0.11$, facilitating quantum control operations.

We compared the measured trapping frequency values with the theoretical extrapolations and observed several interesting deviations from them. Measuring at different DC voltages (Figure 8) revealed that the trapping potential is asymmetric due to the structural asymmetries of the trap, which cannot be neglected. These asymmetries give rise to an additional trapping force induced by the RF ground electrodes. Measurements at different RF and bias voltages (Figures 9 and 10) reveal an unexpected "avoided-crossing" behavior, implying a coupling between V_{rf} and V_{b} quadruples. This phenomenon was studied for the first time only recently, in the context of determining the spatial direction of the trap's principal axes, and still lacks sufficient theoretical modeling. This promising research direction can be further explored in our lab, benefiting our future work and contributing to the field of ion trapping.

This project set the stage for the upcoming steps towards the realization of molecular qubit. As of today, the insights gained from this project, along with the measurement techniques developed to support it, have already been utilized in the successful trapping and identification of our first N_2^+ molecules. In addition,

by tuning the trap to the Lamb-Dicke regime, the motional sideband of the Ca^+ are resolved, allowing high-fidelity qubit transitions to be performed by the soon-to-be-complete 729 nm laser line.

Trapping ions across a wide range of trapping parameters requires careful tuning of the laser cooling parameters. While we have achieved sufficient cooling, further optimization is necessary. By scanning the wavelengths and output powers of the 397 nm and 866 nm lasers, we aim to reach the Doppler cooling limit and identify parameters that maximize photon scattering for optimal detection. The combination of this method with sideband cooling will enable efficient ground-state cooling of Ca^+. Since the molecule is cooled via sympathetic cooling, optimizing the cooling of the atomic ion is a critical step toward achieving molecular quantum control.

References

[1] A. D. Ludlow, M. M. Boyd, J. Ye, E. Peik, and P. O. Schmidt, "Optical atomic clocks", Reviews of Modern Physics **87**, 637–701 (2015).

[2] A. Steane, "Quantum computing", Reports on Progress in Physics **61**, 117 (1998).

[3] D. J. Wineland, "Superposition, entanglement, and raising schrödinger's cat (nobel lecture)", Angewandte Chemie International Edition **52**, 10179–10189 (2013).

[4] H. S. Margolis, "Optical frequency standards and clocks", Contemporary Physics **51**, 37–58 (2010).

[5] F. Wolf, Y. Wan, J. C. Heip, F. Gebert, C. Shi, and P. O. Schmidt, "Non-destructive state detection for quantum logic spectroscopy of molecular ions", Nature **530**, 457–460 (2016).

[6] C.-w. Chou, C. Kurz, D. B. Hume, P. N. Plessow, D. R. Leibrandt, and D. Leibfried, "Preparation and coherent manipulation of pure quantum states of a single molecular ion", Nature **545**, 203–207 (2017).

[7] M. Sinhal, Z. Meir, K. Najafian, G. Hegi, and S. Willitsch, "Quantum-nondemolition state detection and spectroscopy of single trapped molecules", Science **367**, 1213–1218 (2020).

[8] T. Levin and Z. Meir, "Coherent dynamics of a nuclear-spin-isomer superposition", Phys. Rev. Res. **7**, 013274 (2025).

[9] S. Patra, M. Germann, J.-P. Karr, M. Haidar, L. Hilico, V. Korobov, F. Cozijn, K. Eikema, W. Ubachs, and J. Koelemeij, "Proton-electron mass ratio from laser spectroscopy of HD^+ at the part-per-trillion level", Science **369**, 1238–1241 (2020).

[10] S. Alighanbari, G. Giri, F. L. Constantin, V. Korobov, and S. Schiller, "Precise test of quantum electrodynamics and determination of fundamental constants with HD^+ ions", Nature **581**, 152–158 (2020).

[11] M. Tarbutt, "Laser cooling of molecules", Contemporary Physics (2018).

[12] W. Paul, "Electromagnetic traps for charged and neutral particles", Rev. Mod. Phys. **62**, 531–540 (1990).

[13] C. D. Bruzewicz, J. Chiaverini, R. McConnell, and J. M. Sage, "Trapped-ion quantum computing: progress and challenges", Applied physics reviews **6** (2019).

[14] D. Leibfried, R. Blatt, C. Monroe, and D. Wineland, "Quantum dynamics of single trapped ions", Rev. Mod. Phys. **75**, 281–324 (2003).

[15] P. O. Schmidt, T. Rosenband, C. Langer, W. M. Itano, J. C. Bergquist, and D. J. Wineland, "Spectroscopy using quantum logic", Science **309**, 749–752 (2005).

[16] S. Willitsch, "Coulomb-crystallised molecular ions in traps: methods, applications, prospects", International Reviews in Physical Chemistry **31**, 175–199 (2012).

[17] D. J. Wineland, C. Monroe, W. M. Itano, D. Leibfried, B. E. King, and D. M. Meekhof, "Experimental issues in coherent quantum-state manipulation of trapped atomic ions", Journal of Research of the National Institute of Standards and Technology **103**, 259 (1998).

[18] Z. Meir, G. Hegi, K. Najafian, M. Sinhal, and S. Willitsch, "State-selective coherent motional excitation as a new approach for the manipulation, spectroscopy and state-to-state chemistry of single molecular ions", Faraday Discuss. **217**, 561–583 (2019).

[19] Z. Meir, "Dynamics of a single, ground-state cooled and trapped ion colliding with ultracold atoms: a micromotion tale", PhD thesis (Weizmann Institute of Science, 2017).

[20] G. V. Hegi, "Towards a non-destructive single molecular ion state readout and rotational inelastic collisions between molecular nitrogen ions and argon atoms", PhD thesis (University of Basel, 2021).

[21] J. E. Sansonetti and W. C. Martin, "Handbook of basic atomic spectroscopic data", Journal of physical and chemical reference data **34**, 1559–2259 (2005).

[22] D. Lucas, A. Ramos, J. Home, M. McDonnell, S. Nakayama, J.-P. Stacey, S. Webster, D. Stacey, and A. Steane, "Isotope-selective photoionization for calcium ion trapping", Physical Review A **69**, 012711 (2004).

[23] R. Lechner, "Photoionisation of ^{40}Ca with a frequency-doubled 422 nm laser and a 377 nm laser diode", PhD thesis (University of Innsbruck, 2010).

[24] G. Werth, V. N. Gheorghe, and F. G. Major, *Charged particle traps ii* (Springer, 2009).

[25] Z. Meir, T. Sikorsky, N. Akerman, R. Ben-shlomi, M. Pinkas, and R. Ozeri, "Single-shot energy measurement of a single atom and the direct reconstruction of its energy distribution", Physical Review A **96**, 020701 (2017).

[26] R. Saito and T. Mukaiyama, "Determination of principal axes orientation in an ion trap using matter-wave interference", Opt. Express **32**, 42616–42623 (2024).

[27] O. Barnea, D. Einav, J. Drotleff, I. Hochner, and Z. Meir, "Micromotion compensation using dark and bright ions", arXiv:2503.12417 [physics.atom-ph] (2025).